

1 Distance of flight of cosmic-ray muons to study dynamics of the 2 upper muosphere

3
4 Hiroyuki K.M. Tanaka^{1,2*}

5
6 1. University of Tokyo, Tokyo, Japan.

7 2. International Virtual Muography Institute (VMI), Global, Tokyo, Japan.

8
9 Correspondence to: Hiroyuki K.M. Tanaka

10
11 *email: ht@eri.u-tokyo.ac.jp

12 13 14 **Abstract**

15 The Earth can be divided by main layers, including the atmosphere, geosphere (solid
16 Earth), and biosphere, depending on its predominant component. In this work, the layer
17 of the Earth which constantly contains a high concentration of muons ($\sim 8 \times 10^{12}$ muons)
18 and its upper border are respectively defined as the muosphere and muopause. The
19 altitude of the muosphere spans from the lower stratosphere to the upper crust of the Earth.
20 In order to study its dynamics, the muopause height was spatiotemporally studied with a
21 new kind of technique called the distance of flight (DOF) which utilizes variations in the
22 muon's decay length. In this work, (A) numerical modeling was performed, and it was
23 clarified that seasonal variations in the cosmic muon flux are predominantly ruled by
24 muopause dynamics, (B) the muon data were compared with the balloon-based
25 measurement results, and it was confirmed that muopause dynamics is closely related
26 with lower-stratospheric height variations. Since the muopause is the region spanning
27 between the upper troposphere and the lower stratosphere, the potential of the current
28 distant of flight (DOF) approach needs to be further investigated by cross-comparing
29 related case studies and other atmospheric climate datasets.

30 31 **Introduction**

32 Muons are secondary particles generated in the Earth's atmosphere as a result of hadronic
33 interactions between the incident primary cosmic rays (primaries) and atmospheric nuclei
34 such as nitrogen and oxygen. These primaries rarely interact with matter within the top

35 region of the Earth's atmosphere due to the low number density of atmospheric nuclei.
36 However, as primaries' injection depth increases, the density of the atmosphere increases,
37 and these primaries increasingly interact with nuclei, producing mesons such as charged
38 pions and kaons which eventually decay into muons. Once these mesons decay into
39 muons, there will generally be no further interaction to generate new particles since
40 muons do not strongly interact with matter since muons undergo only electromagnetic
41 and weak interactions but not strong nuclear interactions. Therefore, muons are
42 extensively produced within particular altitude regions of the atmosphere. The muons'
43 production rate increases as a function of the atmospheric depth such that: <0.01%, ~0.2%,
44 ~2%, ~30%, and ~80% (of the entire muons we observe at sea level) up to an atmospheric
45 depth of 5 hPa, 10 hPa, 50 hPa, 100 hPa, and 200 hPa, respectively, and almost all muons
46 are generated up to an atmospheric depth of 300 hPa (Particle Data Group, 2022; Boezio
47 *et al.*, 1999; Boezio *et al.*, 2000). On the other hand, due to their strong penetration power,
48 the muons also exist in the geosphere with a rock/water depth up to ~5/~10 km.
49 Consequently, muons are predominant in the region defined on the altitude coordinate as
50 ranging from 30 km and -10 km which also partly overlaps with regions of the
51 humanosphere. This region (from +30 km to -10 km from sea level) is here defined as
52 the muosphere. Accordingly, the muopause is defined as the upper boundary of the
53 muosphere (as with the tropopause defining the upper boundary of the troposphere) which
54 is located at 30 km asl. The key characteristics of the muons within the muosphere are:
55 (A) an abundance of $\sim 8.0 \times 10^{12}$ muons* with the number of $\sim 5 \times 10^3$ muons km^{-3} are
56 constantly present in the muosphere, (B) $\sim 8 \times 10^{16}$ muons are generated in the muosphere
57 every second and (C) $\sim 5 \times 10^{16}$ muons arrive at sea level every second. The exception to
58 this would be neutrino-induced muons which exist throughout the geosphere (Particle
59 Data Group, 2022), but the number of these neutrino-induced particles within the
60 geosphere is too small ($< 10^{-9}$ muons km^{-3}) to categorize them as being part of the
61 muosphere.

62

63 $*(1.6 \times 10^2 \text{ m}^{-2}\text{s}^{-1})$ [averaged muon flux] $\times (5 \times 10^{14} \text{ m}^2)$ [Earth's surface area] $\times (3.0 \times 10^4$
64 $\text{ m})$ [thickness of the muosphere] / $(3 \times 10^8 \text{ ms}^{-1})$ [speed of muons]

65

66 The thickness of the muosphere spatiotemporally fluctuates due to processes near the
67 surface of the Earth: mainly crustal deformation and land temperature variations. Crustal
68 deformation alters the density of the shallow crust and local topography. When this occurs,
69 the underground depth threshold for muons to reach will be altered; hence the position of
70 the bottom part of the muosphere is regionally altered, but the time scale of this change

71 is very long (over millennia). On the other hand, the near-surface temperature variations
72 will alter the isobaric surface height near the muopause in much shorter time scales.

73

74 Since muopause height variations are closely related with the upper-tropospheric and
75 lower-stratospheric isobaric surface height variations, studying muopause dynamics has
76 the potential to contribute to research in this field. For example, it was reported that the
77 2020 and 2021 ozone holes were both associated with large decreases in polar lower
78 stratospheric heights (Yook *et al.*, 2022). Sudden stratospheric warming (SSW) is
79 characterized by large isobaric surface height rises at the pole (Kretschmer *et al.*, 2018).
80 The 2022 Hunga Tonga–Hunga Ha’apai volcano eruption, Tonga resulted in a substantial
81 injection of water vapor into the upper atmosphere (Millán *et al.*, 2022; Vömel *et al.*,
82 2022). Such changes in the atmospheric composition should have had a noticeable impact
83 on the muopause.

84

85 The established muographic imagery techniques have been applied to natural phenomena
86 such as volcanoes (Tanaka *et al.*, 2014), cultural heritage (Morishima *et al.*, 2017), tropic
87 cyclones (Tanaka *et al.*, 2022a), meteotsunami (Tanaka *et al.*, 2022b), and contraband
88 detection (Gnanvo *et al.* 2011). These techniques take advantage of known properties of
89 muon transmission and scattering through matter. In this work, the DOF technique is
90 added, and it will be shown that the muopause height variations can be measured with
91 this technique based on the quantitative analysis of the time-sequential muon data. Since
92 muons are leptons with a lifetime at rest is 2.2 microseconds, the actual lifetime as
93 observed from the detector, and therefore the path traveled, is much longer by the
94 relativistic time dilation factor, and that the latter depends on energy. Consequently, the
95 sea-level muon flux will decrease/increase as the muopause uplifts/lowers. This is the
96 basic principle of the DOF approach. In this work, the aim was to show balloon-based
97 lower stratospheric height variations are well reproduced by applying the DOF approach
98 to the time-sequential muon observation data.

99

100 There are a number of reports exploring barometric and temperature effects in the muon
101 flux (Tanaka *et al.*, 2022a; Tilav *et al.* 2010; COSINE-100 Collaboration, 2020;
102 Myssowsky and Tuwim *et al.* 1926; Blackett, 1938; The IceCube Collaboration, 2019;
103 Adamson *et al.*, 2010; Tramontini *et al.*, 2019; Blumer *et al.*, 2005; Dmitrieva *et al.* 2011).
104 However, many of these works focus on either tropospheric barometric effect or
105 stratospheric temperature effect. In this work, DOF approach was modeled and applied
106 to the 1,044-day time sequential muon data to compare with the Japan Meteorological

107 Agency's balloon data.

108

109 As a result, the following two major characteristics were identified: (A) seasonal
110 variations in the muon flux due to the isobaric surface height effect are much larger than
111 seasonal variations due to the barometric effect, therefore, (B) the isobaric surface height
112 derived by the DOF technique is consistent with the balloon-based upper-atmosphere
113 isobaric surface height measurement results. In this paper, a detailed description of the
114 process to arrive these results is provided. A brief discussion of its current limitation and
115 potential improvements are also described.

116

117 **2. Muosphere and muopause**

118 If the *abundant muon flux* is defined as ≥ 10 muons $\text{m}^{-2}\text{s}^{-1}\text{sr}^{-1}$, the abundant muon flux is
119 available within the altitude region between 24.5 km above sea level (a.s.l) to 20 m below
120 ground surface of 40 m below sea level (b.s.l). This space is hereafter defined as the
121 "middle muosphere". The region where muons exist above the middle muosphere is
122 called the upper muosphere, and the region where muons exist below the middle
123 muosphere is called lower muosphere. The muon flux available in the middle muosphere
124 and the lower muosphere on the Earth are summarized in Table 1. Vertical classification
125 of the muosphere is shown in Figure 1 as a function of the available muon flux. The
126 muopause is defined as the altitude region with the highest muon generation rate per unit
127 atmospheric depth (dI/dX , where I is the muon flux, and X is the atmospheric depth).
128 dI/dX takes maximum is ~ 21.5 km a.s.l. where a muon flux increases by ~ 40 $\text{m}^2\text{s}^{-1}\text{sr}^{-1}$
129 every 1 km atmospheric depth. (Figure 2). This peak is defined as the *specific muopause*.
130 If the width of the muopause is defined the region where $dI/dX \geq 20$ $\text{m}^2\text{s}^{-1}\text{sr}^{-1}\text{km}^{-1}$ (half
131 maximum), the muopause spans from 18 km a.s.l. to 24.5 km a.s.l. This muopause is
132 defined as the *full-width half-maximum (FWHM) muopause*. The middle muosphere
133 contains both atmospheric and geospheric layers.

134

135

136

137

138

139

140

141

142

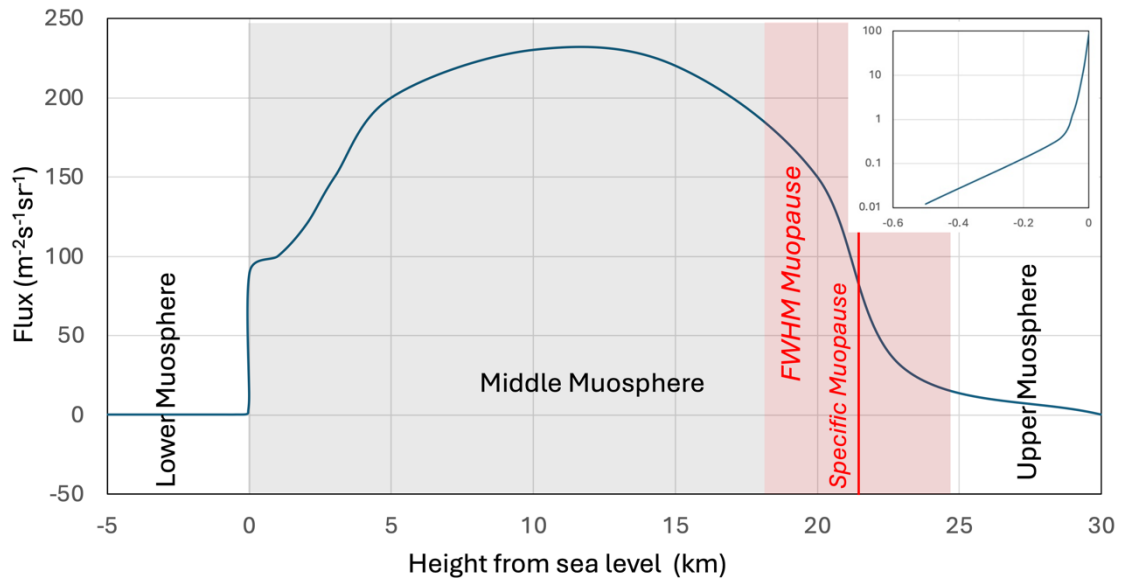
143
 144
 145
 146
 147
 148
 149
 150
 151
 152
 153
 154
 155
 156
 157
 158
 159
 160
 161
 162
 163
 164
 165
 166
 167
 168
 169
 170
 171
 172
 173
 174
 175

Table 1. Available muon flux in the middle muosphere and the lower muosphere on the Earth. The data were taken from Particle Data Group (2022).

Height (km)	Muon flux ($\text{m}^{-2} \text{sr}^{-1} \text{s}^{-1}$)
Upper Muosphere 30	$<10^{-2}$
-	
25	1.0×10^1
23	3.0×10^1
20	1.5×10^2
15	2.2×10^2
10	2.3×10^2
5.0	2.0×10^2
3.0	1.5×10^2
2.0	1.2×10^2
1.0	1.0×10^2
Sea level	9.0×10^1
-0.02	1.0×10^1
-	
-0.05	2.8×10^0
-0.01	3.2×10^{-1}
-0.5	1.2×10^{-2}
-1.0	1.2×10^{-3}
-2.0	7.0×10^{-5}
-3.0	6.0×10^{-6}
-4.0	6.0×10^{-7}
-5.0	7.0×10^{-8}

Atmosphere

Geosphere

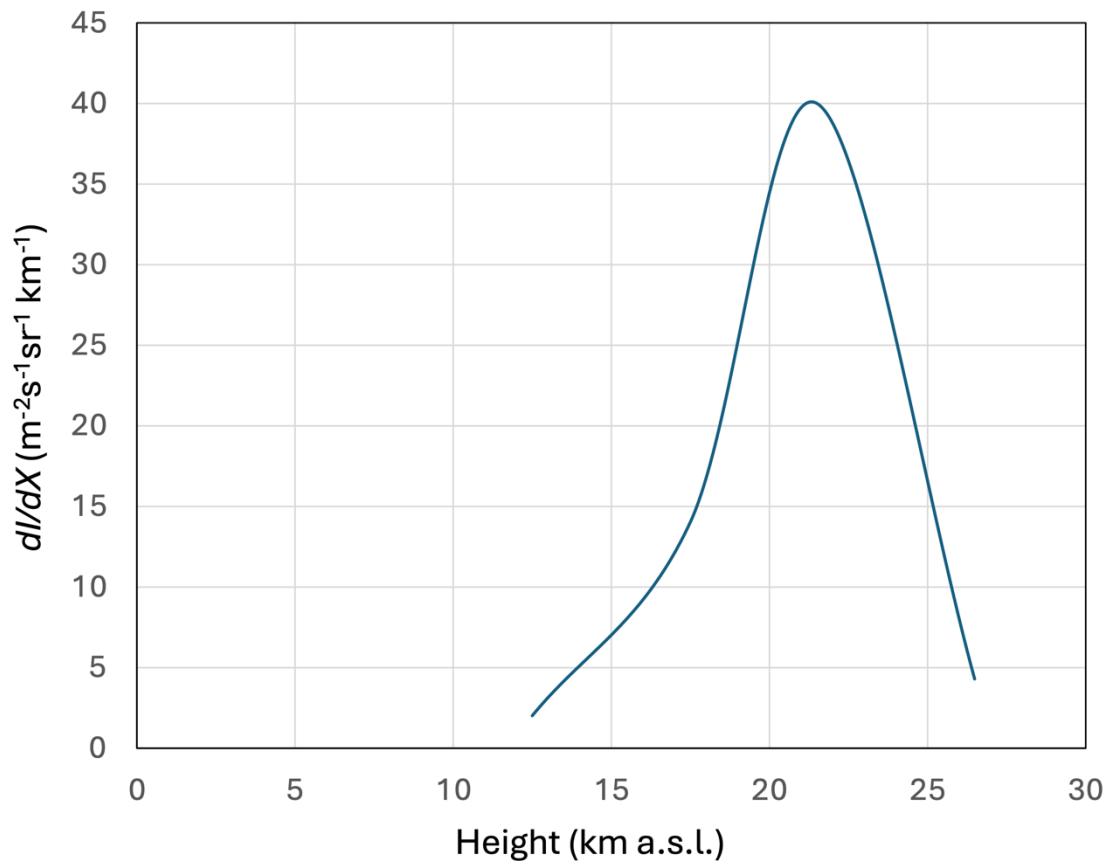


176

177 Figure 1. Configuration of the muosphere. The gray and red shaded areas respectively
 178 indicate the middle muosphere, and the FWHM muopause. The vertical red line indicates
 179 the location of the specific muosphere. The inset indicates a magnified view in the vicinity
 180 of the interface between the middle muosphere and the lower muosphere.

181

182



183

184 Figure 2. Muon flux gradient as a function of the altitude.

185

186 The proposed DOF technique is similar to ground-based atmospheric LiDAR in terms of
 187 scanning the upper atmosphere. Muons are generated most extensively at the muopause
 188 that spans from the upper troposphere to the lower stratosphere. If the tropopause shifts
 189 upward, this density gradient shifts upward accordingly, and accordingly, the muopause
 190 shifts upward, then the muon's travel distance increases. The current technique measures
 191 the height of where muons are extensively generated; hence the height of the tropopause
 192 by measuring the muon's DOF. For this aspect, the DOF technique measures the dynamic
 193 (PV) tropopause height variations indirectly. (UV LiDAR measures the O₃ tropopause,
 194 and visible light LiDAR measures the cirrus cloud.) Due to the muon's strong penetrating
 195 capability, the DOF technique is not influenced by the cloud existence.

196

197

198 **2. Principle of the DOF technique**

199 The atmospheric cascades of secondary pions and kaons are developed as a result of the
 200 competition between hadronic collisions of mesons with nuclei and the decay process of

201 the mesons in the atmosphere. Therefore, muons are not generated at a specific altitude,
202 but instead they are generated within a certain altitude range (Boezio *et al.*, 1999; Boezio
203 *et al.*, 2000).

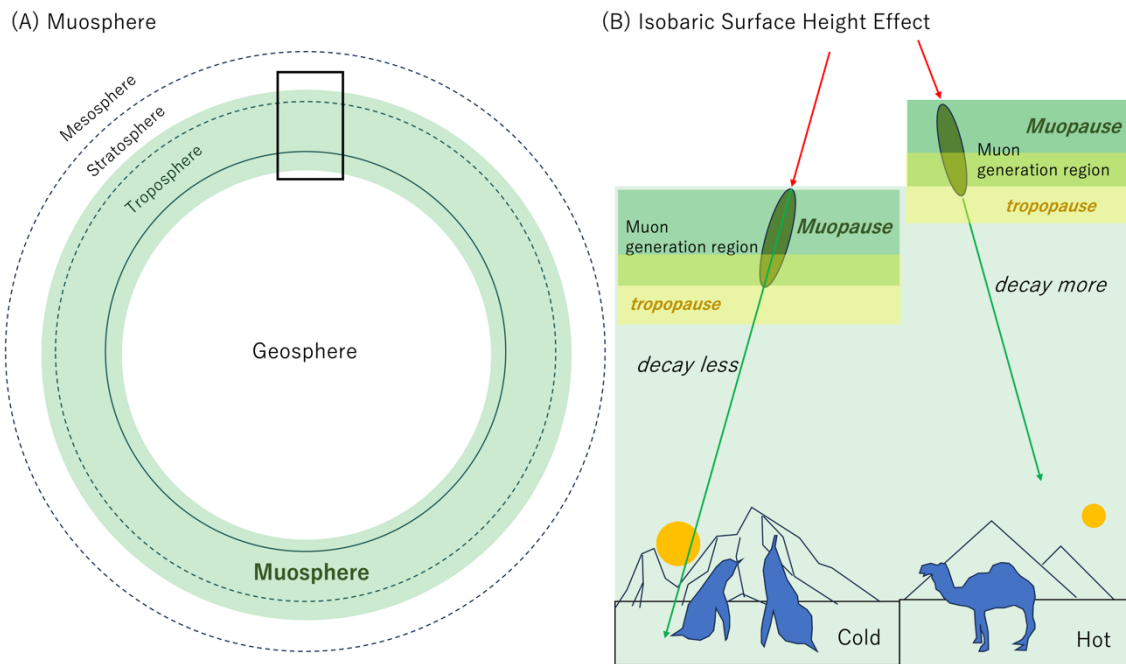
204

205 Figure 3 shows the layer span of the muosphere on the Earth and the principle of the DOF
206 technique. As shown in Figure 3A, the muosphere covers the region from the lower
207 stratosphere, troposphere, and shallow region of the geosphere (shallow crust and ocean).
208 Topography of the muopause is determined by the isobaric surface height distribution of
209 the upper atmosphere, and is generally related to the height of tropopause. However, the
210 tropopause region does not usually overlap with the muopause region. The isobaric
211 surface height is high when the surface temperature is high and low in when the surface
212 temperature is low since the larger vertical temperature gradient causes deeper convection
213 in the troposphere, pushing the isobaric surface, upwards; hence seasonally varied. More
214 detailed descriptions can be found later in the “Balloon-based studies near the muopause”
215 section. As shown in Figure 3B, variations in the height of the muopause will affect the
216 muon generation point; hence the muon’s DOF. The number of muons decreases when
217 the muopause is uplifted. If the isobaric surface height effect is comparable to or stronger
218 than the barometric effect on the muon flux, the spatiotemporal variations in the
219 muopause can be measured by using the local barometric data. Detailed descriptions
220 about two essential aspects of the DOF technique, (1) modelling of the seasonal
221 barometric effect on the muon flux and (2) modelling of the seasonal isobaric surface
222 height effect on the muon flux, are given in the following subsections.

223

224 There are three effects that influence the muon flux: (A) variations in the muon's range
225 due to barometric variations, (B) variations in the muopause height due to variations in
226 mass exchange between the upper troposphere and the lower stratosphere; hence
227 variations in the muon's distance of flight between the muopause and sea level, and (C)
228 variations in hadronic interaction mean free paths due to stratospheric temperature
229 variations. There are three effects in total. Effect (C) comes from the competition between
230 the pion’s and kaon’s hadronic interaction mean free path (MFP) and decay length. If the
231 stratospheric temperature increases, the air thermally expands and thus, the hadronic
232 interaction MFP increases. However, this effect is much smaller than the other two effects
233 since this factor is only relevant for muon flux in the energy region above 50 GeV
234 (IceCube Collaboration, 2019) where the integrated muon intensity is lower by more than
235 2 orders of magnitude. Effect (A) includes variations in the muon’s stopping power due
236 to variations in their energy loss rate in the atmosphere, and variations in the muon’s

237 decay length due to variations in their deceleration rate in the atmosphere. While there
 238 have been several works investigating the Earth's atmosphere using muons, using effect
 239 (A) (Tanaka *et al.*, 2022b; Tramontini *et al.* 2019), these previous works focused on
 240 gauging areal density variations (convertible to temperature and pressure) of the
 241 atmosphere which is conceptually close to muographic imagery. On the other hand, the
 242 DOF technique inversely using the effect (B) has never been attempted.
 243
 244



245
 246 Figure 3. Definition of muosphere and the principle of the DOF technique. The span of
 247 the muosphere is shown along with other layers of the Earth (A). The black box indicates
 248 the muosphere for the region shown in (B). Red arrows and green arrows respectively
 249 indicate the primary cosmic rays and muons. Additionally, (B) shows an example of the
 250 contrast between the average height of the muopause above colder surface temperature
 251 and the height of the muopause above warmer surface temperature. Dark green ovals
 252 indicate the muon production regions. As is indicated with yellow-filled boxes, the
 253 tropopause and the muopause do not exactly overlap with each other.
 254
 255

256 3. DOF Modeling

257 3.1 Modeling of the seasonal barometric effect on muon flux

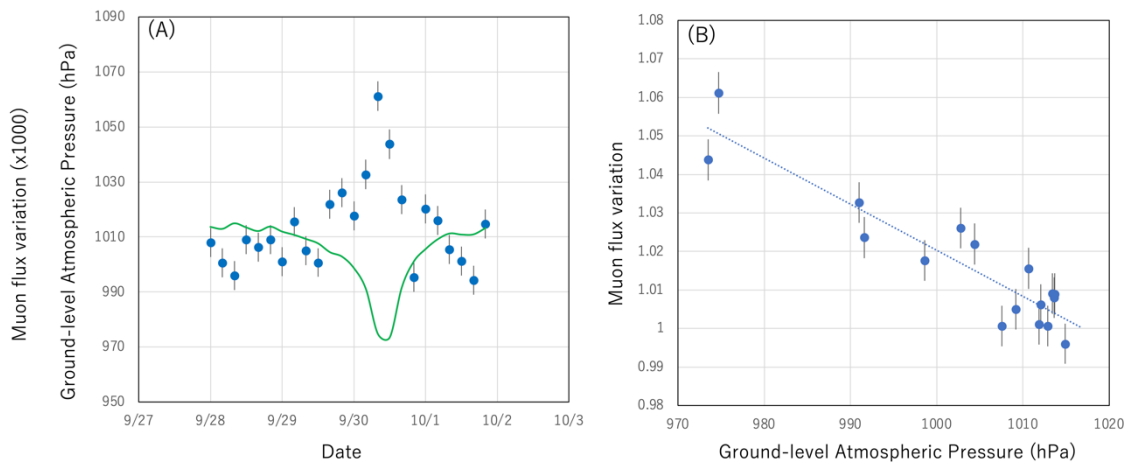
258 The cosmic muon flux is also influenced by ground-level barometric variations because
 259 the amount of muon energy loss depends on the total areal density along their trajectories.

260 In this work, we took advantage of muon flux variations associated with the presence of
261 a cyclone to derive variations in the muon counts in the detector as a function of the
262 ground-level pressure in Kagoshima city. The advantage of using the cyclone data is that
263 since the cyclone moves quickly (typically within 24 hours) and will dramatically alter
264 the ground-level atmospheric pressure (sometimes by more than 40 hPa), barometric
265 muon flux variations can be evaluated without being influenced from the longer-time-
266 scale isobaric surface height effect. According to Tanaka *et al.* (2022a), the barometric
267 correction of the muon flux can be reasonably performed by using the tropic cyclone
268 passage events. Their reported flux drop rate is 0.0016/hPa (theory) and 0.001/hPa -
269 0.002/hPa (observation). This flux drop rate includes (A) the flux drop due to the higher
270 rate of muon's absorption into the atmosphere (stop and decay), and the flux drop due to
271 an increase in inflight decay of muons (since they lose their energy more). Figure 4A
272 compares the temporal variations in the muon flux and the temporal variations in the
273 ground-level atmospheric pressure induced by the 2018 Typhoon No 24. Figure 4B shows
274 the relationship between the muon flux and the atmospheric pressure (both measured in
275 Kagoshima city). The metrological data in Figure 4A were taken from Reference (Japan
276 Metrological Agency, 2023). The data points in Figure 4B were fitted by a linear function
277 and the result is shown in the following equation:

$$278 \Delta N = -0.0012 \Delta P [\text{hPa}] + 2.2159. \quad (1)$$

280
281 This result indicates that the muon flux varies by 1.2% if the ground-level atmospheric
282 pressure changes by $\Delta P = 10$ hPa (with respect to 1,000 hPa). Since the detector used for
283 measuring this cyclone effect on the muon flux is identical to that used for the DOF
284 measurements, the external factors including the zenith angular dependence of the muon
285 flux, geometrical acceptance of the detector, etc. are canceled out. The fractions of the
286 number of the data points are respectively 60%, 82%, and 100% for deviations of $\leq 1\sigma$,
287 $\leq 1.5\sigma$, and $\leq 2\sigma$ from the estimated line. The SD of the data points from the estimated line
288 (6.5×10^{-4}) is close to the statistical error associated with the data points (5.2×10^{-4} - 5.4
289 $\times 10^{-4}$). The R^2 value (coefficient of determination) for this fitting was 0.85. The current
290 result (0.00055/hPa -0.00185/hPa) in agreement with the flux drop rate reported in the
291 prior work (0.001/hPa -0.002/hPa) within the error bars. The difference between them
292 (0.0037) can be the fitting uncertainty which adds an uncertainty of ~ 18 m in estimation
293 of the muopause height (See below). Eq. (1) was used for the barometric correction to the
294 muon flux in the current work.

295



296

297

298

299

300

301

302

303

304

305

306

307

308

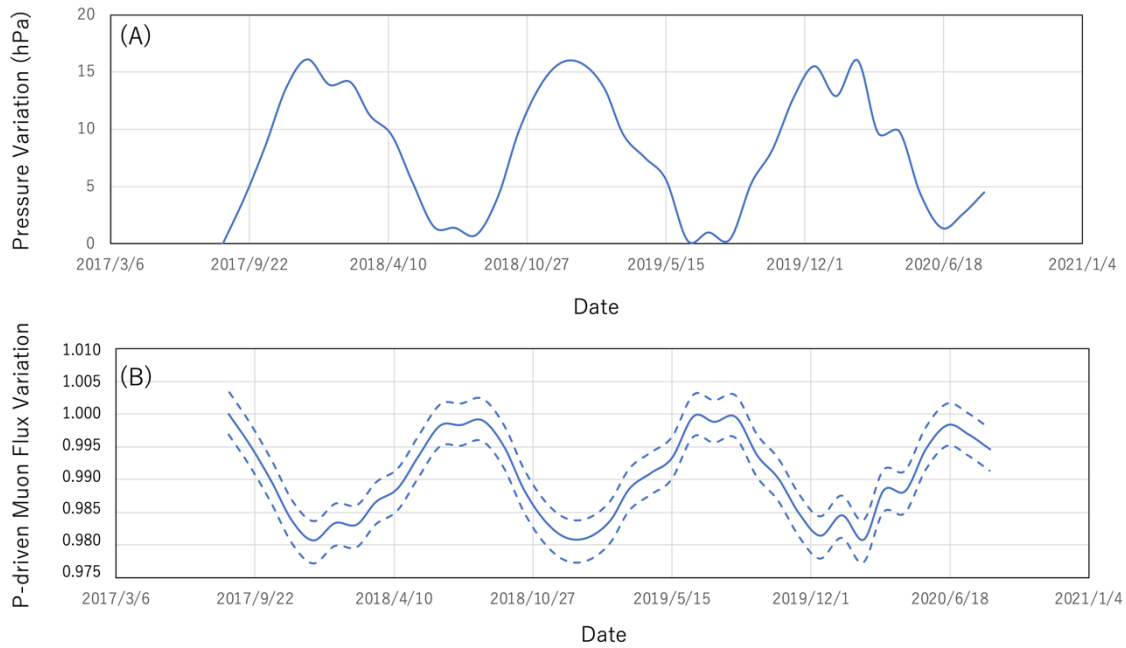
309

310

311

Figure 4. Variations in the muon flux induced by the ground-level atmospheric pressure variations. The muon flux variations (blue filled circles) are compared with the ground-level atmospheric pressure variations (green solid lines) induced by the 2018 Typhoon No 24 (A). The muon flux variations (blue filled circles) are shown as a function of the ground-level atmospheric pressure. The numbers on the vertical axis indicate the muon flux variation times 1,000. The dotted line indicates the linear function fitted to these data points (B).

With Eq. (1), seasonal variations of the muon flux caused by variations in the ground-level atmospheric pressure (P-driven muon flux variations) were evaluated. Figure 5A shows seasonal variations in the ground-level atmospheric pressure measured at the Kagoshima Meteorological Observatory in the period between August 2017 and August 2020. Figure 5B shows the corresponding P-driven muon flux variations based on Eq. (1).



312
 313 Figure 5. Seasonal variations in the ground-level atmospheric pressure (A) and estimated
 314 variations of muon flux due to variations in the ground-level atmospheric pressure (B)
 315 based on Eq. (1). The data are shown in the period between August 2017 and August
 316 2020. The ground-level atmospheric pressure data were taken from Reference (Japan
 317 Metrological Agency, 2023). The area between dashed lines in panel (B) indicates the
 318 barometric modeling error (1 S.D.) The error values associated with the barometric data
 319 are not published by Japan Metrological Agency.

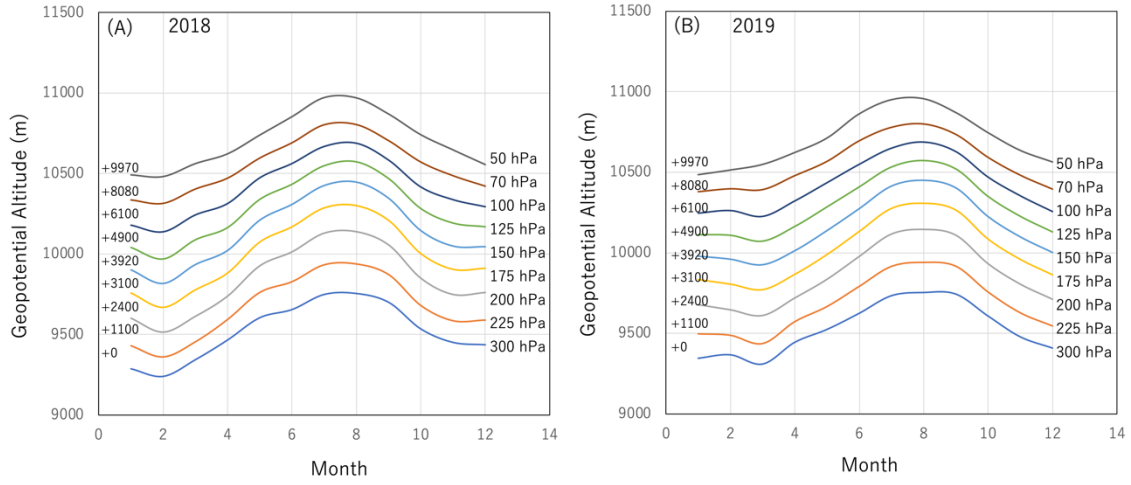
320

321

322 **3.2 Balloon-based studies of the isobaric surface height near the muopause**

323 Japan Meteorological Agency launches a balloon from Kagoshima city twice a day (09:00
 324 and 21:00 JST) to monitor the isobaric surface height of the upper atmosphere. The
 325 monthly isobaric surface height measurement results acquired in 2018 and 2019 are
 326 shown in Figure 6. As shown in this figure, the altitude of the muopause varies $\Delta H \sim 500$
 327 m, reflecting seasonal variations (i.e., altitude that increases in the summer time) of the
 328 muopause. While the muon generation depth has a certain span (50-300 hPa), as can also
 329 be seen in this figure, the isobaric surface height corresponds closely with the variations
 330 in this span. Therefore, we can conclude that the isobaric structure of the upper muosphere
 331 is simply pushed further from sea level in summer and pushed closer to sea level in winter
 332 (dark green ovals in Figure 3B). Consequently, it is expected that variations in the muon
 333 survival rate at sea level is a function of the muopause height.

334



335

336 Figure 6. Seasonal changes in the isobaric surface height of the upper troposphere and the
 337 lower stratosphere. The data acquired in 2018 (A) and the data acquired in 2019 (B) are
 338 shown. The data were taken from the Japan Metrological Agency survey (Japan
 339 Metrological Agency, 2023). The numbers on the left side of each panel indicate the offset
 340 of the altitude in units of meters.

341

342

343 3.3 Modeling of the seasonal isobaric surface height effect on the muon flux

344 As was described in the previous subsection, the isobaric surface height variations ΔH
 345 (H) are independent from H in this span. The modeling procedure is summarized as
 346 follows.

347

348 (A) The zenith-angular dependent open-sky muon spectrum data points are taken from
 349 various prior experimental works (Allkofer *et al.*, 1985; L3 Collaboration., 2004).

350

351 (B) These muon spectrum data points are interpolated to derive $I_0(E, \theta)$ by using the
 352 Thompson and Whalley analytical formula (Thompson and Whalley, 1977).

353

354 (C) Calculations of the angular-dependent muon flux are done, based on the following
 355 formula:

356

$$357 \quad n(\theta, \phi) = \int I(E, \theta) dE, \quad (2 - 1)$$

358

$$359 \quad I(E, \theta) = I_0(E, \theta) \exp[-\Delta H(\sin \theta)^{-1} (c \tau \gamma)^{-1}] (1 - \Delta N), \quad (2 - 2)$$

360

361 where E and θ are respectively the muon's energy, τ is the muon's decay constant, and
362 the arrival angle from zenith at sea level, $I_0(E, \theta)$ is the reference muon flux, and γ is the
363 Lorentz factor. In Eq. (2.2), reduction of E is calculated by assuming the fixed
364 atmospheric pressure (1013 hPa), and the effect of temporal barometric variations on
365 dE/dX was neglected since the decay effect coming from the muon's energy loss
366 variations due to temporal barometric variations is already incorporated into ΔN .
367 Moreover, this decay effect in seasonal variations is small. For example, there is 15 hPa
368 barometric variations between winter and summer (Figure 3), and these variations induce
369 variations in energy loss of 30 MeV (in vertical), which extend/contract the muon's decay
370 length by 190 m (in vertical) which is smaller than the muopause height variations by a
371 factor of 3 (Figure 6). Radiative processes (i.e., bremsstrahlung, direct pair production,
372 and photonuclear interactions) in dE/dX were neglected due to relatively long radiation
373 length in air. Figure 7 plots Eq. (2-1) for $\Delta H = 0$ m (Figure 7A) and $\Delta H = +500$ m (Figure
374 7B). The data points are overlaid on this plot. Although it is difficult to estimate ΔH
375 when these data were gathered, but it is assumed that $\Delta H = 0$. It is important to note that
376 in the current work, the quantity to be evaluated is variations in H , not H itself. The
377 positive and negative signs attributed to ΔH respectively indicate respectively upward
378 variations and downward variations. If θ approaches the value of 90° , $(\cos\theta)^{-1}$ will be
379 diverged, so in this case, the spherical curvature of the Earth has to be considered (for θ
380 $\sim 90^\circ$).

381

382 (D) Calculate the number of muons recorded by the detector with:

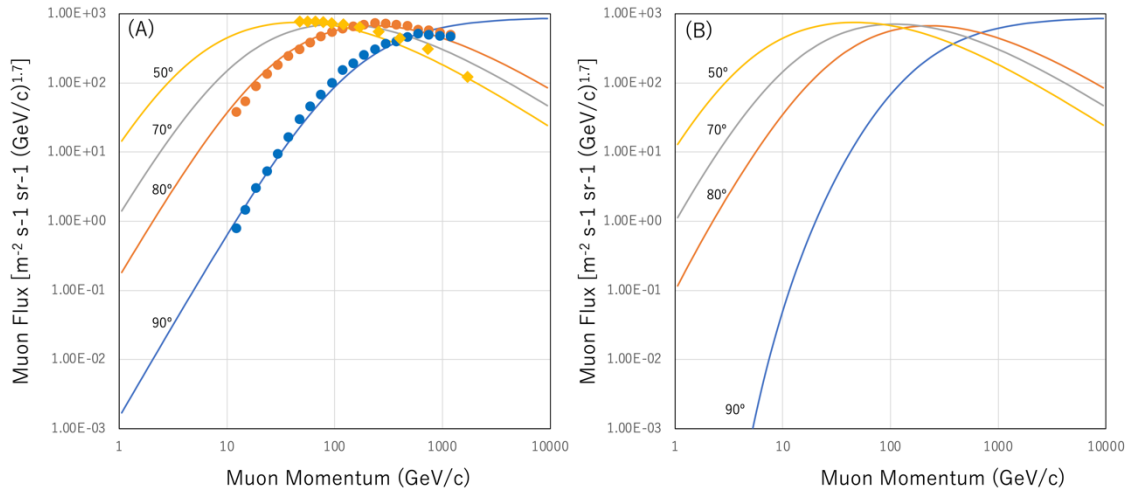
383

$$384 \quad N = \int_{\phi_0}^{\phi_1} \int_{\theta_0}^{\theta_1} n(\theta, \phi) d\theta d\phi, \quad (3)$$

385

386 where θ_0 , θ_1 , ϕ_0 , and ϕ_1 are respectively the detector's zenith (θ_0 - θ_1) and azimuth (ϕ_0 - ϕ_1)
387 angular acceptance. Eq. (3) was used for the isobaric correction to the muon flux in the
388 current work.

389



390

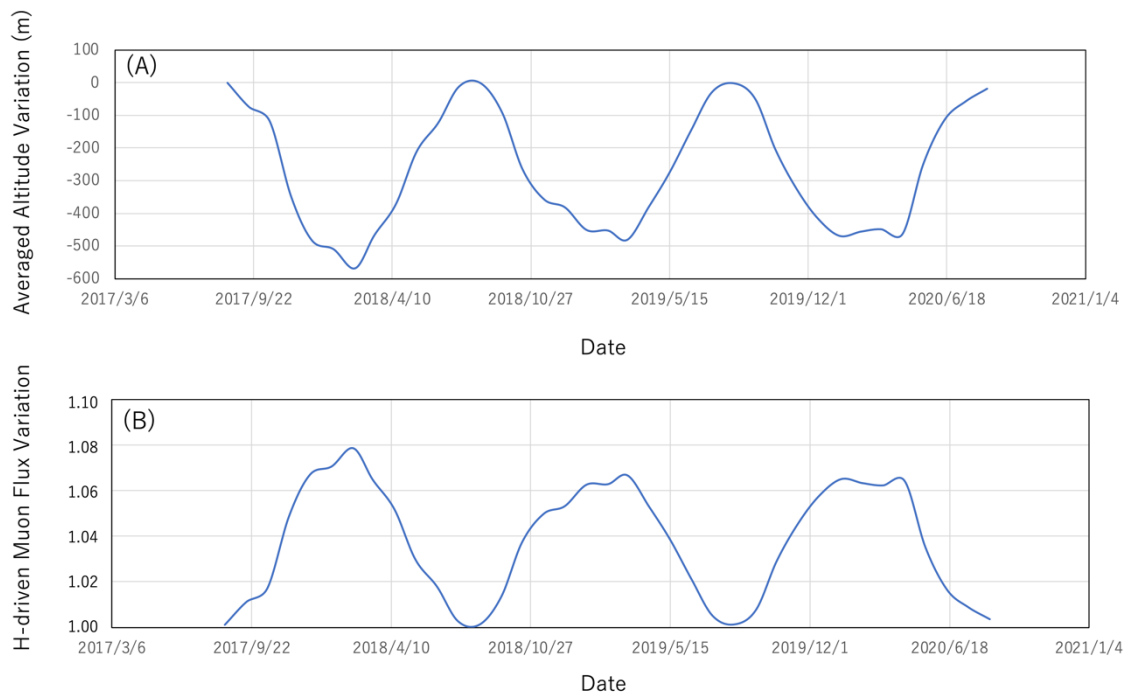
391 Figure 7. Differential muon flux for different isobaric surface altitudes. The spectra
 392 calculated for the reference isobaric surface altitude ($\Delta H = 0$ m) are shown in (A) and for
 393 the case when the isobaric surface is uplifted by 500 m in (B) for various muon's arriving
 394 angles: 90° (blue), 80° (orange), 70° (gray), and 50° (yellow). Only slanted muons are
 395 shown due to the geometrical configuration of the current detector setup (see below).
 396 Filled circles and filled rhombuses are respectively the data points taken from Allkofer *et*
 397 *al.* (1985) and L3 Collaboration (2004).

398

399

400 With Eq. (2-1), seasonal variations of the muon flux due to the isobaric surface height
 401 effect (H-driven muon flux variations) were calculated. Figure 8A shows the balloon-
 402 based ΔH value averaged over the altitudes which ranged between 50 hPa and 300 hPa.
 403 Figure 8B shows the corresponding H-driven muon flux variations based on Eq. (2-1). In
 404 order to match the angular acceptance of the tracker (described in the next section), the
 405 zenith-angular integration range of Eq. (2-1) was set to be 50° - 90° . It was assumed that
 406 the muon's arriving angles are azimuthally isotropic. These results are subsequently used
 407 for the muon flux modeling process which will be described in the following subsection.
 408 As can be compared between Figure 5 and Figure 8, the seasonal isobaric surface height
 409 effect (up to 8%) is much larger (by a factor of 4) than the seasonal barometric effect (up
 410 to 2%).

411



412
 413 Figure 8. Balloon-based isobaric height variations averaged over the altitudes between 50
 414 hPa and 300 hPa (A) and H-driven variations of the muon flux without the barometric
 415 correction (B). The data are shown for the period between August 2017 and August 2020.
 416 The balloon-based isobaric height data were taken from Japan Metrological Agency
 417 (2023) The error values associated with the balloon data are not published by Japan
 418 Metrological Agency.

419
 420

421 **4. Apparatus**

422 The muon tracker used in this study consisted of 90 scintillator strip detectors. Each
 423 scintillator strip detector consisted of a plastic scintillator (Eljen EJ-200) strip connected
 424 to a photomultiplier tube (PMT; Hamamatsu R7724) via an acrylic light guide. The
 425 typical pulse height outputted from the PMTs were 3-5 V while the threshold level of the
 426 discriminator was set to be 50 mV, so that the counting rate would not be easily influenced
 427 by the drift of the PMT gain and the discriminator's threshold level caused by variations
 428 in ambient temperature. The width and the length of the plastic scintillator strip were
 429 respectively 100 mm and 1500 mm. These strips were arranged vertically and horizontally
 430 to form three position sensitive detectors (PSDs). Three PSDs were vertically arranged
 431 with a spacing of 60 cm. In order to reject electromagnetic components, such as
 432 positrons/electrons a 10-cm thick lead slab concealed inside a 1.5 cm thick stainless-steel
 433 case (totaling 3 cm in thickness) were inserted into each interval between the PSDs. A

434 stainless-steel case is needed to protect the lead for the following reasons: (A) lead is soft,
435 and for long-time measurements, it can be deformed, so it has to be supported by the
436 stainless-steel case, and (B) lead is poisonous, not allowed to use it outdoor environments
437 without coverage, so it has to be covered by the stainless-steel box.

438

439 The best way to check the long-term detector stability is to use IBE (inverse barometric
440 effect). Barometric variations in the muon flux are compensated by the tidal height
441 variations since the total areal density above the detector will be constant as long as the
442 detector is located undersea, so that the local fluctuations due to barometric variations can
443 be intrinsically removed from the data without any artificial actions. According to the
444 data taken at the Trance Tokyo-bay Aqua Line undersea tunnel, Japan, variations in the
445 lunar daily muon rate was ~ 0.0028 (S.D.) including stactical errors of ~ 0.001 (S.D.) for
446 half-year measurements (Tanaka *et al.* 2021). The detector had the same configuration
447 used in this work (R7724 and EJ200).

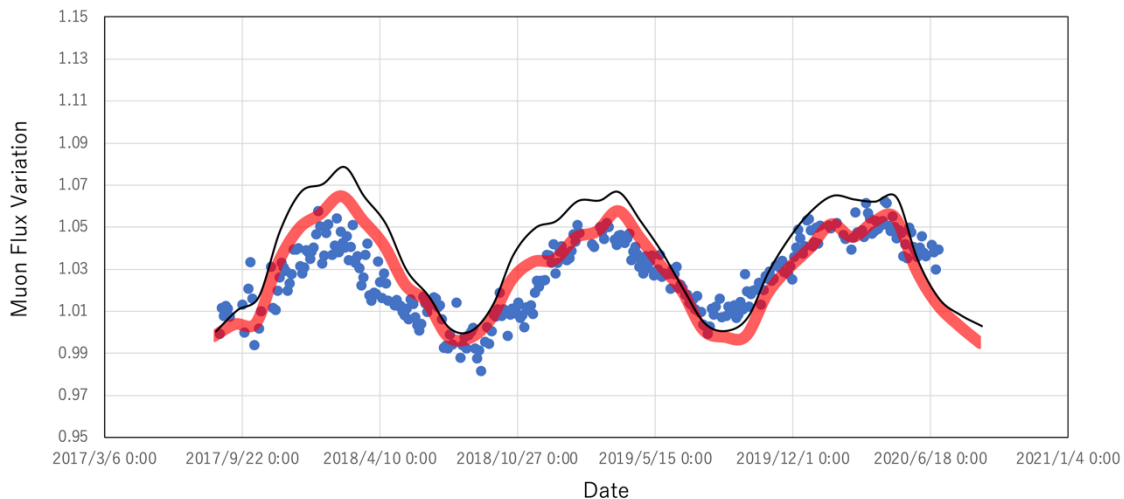
448

449 Each of the resultant PSDs consists of a segmented plane with 15×15 segments having
450 a 1.5×1.5 m² active area with a spatial resolution of 10 cm. Since the distance between
451 the uppermost stream detector and the lowermost stream detector is 120 cm, the angular
452 resolution of this detector is 83 mrad. This angular resolution is equivalent to the spatial
453 resolution of 830 m at a location 10 km from the tracker, but it is reduced to 8.3 km at a
454 location 100 km from the tracker. The elevation and azimuth angular acceptance are
455 respectively $0^\circ - 51^\circ$ and $\pm 51^\circ$. However, since the active area is drastically reduced for
456 muons injecting at higher angles with respect to PSD planes (e.g., for muons arriving at
457 an elevation angle of 51° and an azimuth angle of 51° , the tracker's active area is reduced
458 to $1/225$), for practicality, a much smaller angular region ($14^\circ - 32^\circ$ for elevation angular
459 region and $\pm 28^\circ$ for azimuthal angular region) was employed. For tracking, all vertices
460 are examined but only the vertices that are aligned (along a straight line) are counted as
461 an event to ensure that only muons were selected. Lead and stainless-steel shields within
462 the detector decrease the background noise, however they also increase the possibility of
463 muon scattering events. However, these scattering angles (10-20 mrad) are considered to
464 be negligible in comparison to the current tracker's angular resolution (>80 mrad). The
465 muon tracker used in the current experiment was located in Kagoshima city, Japan and it
466 was pointed towards the southern direction. The measurement period was between
467 August 20, 2017- June 30, 2020 (1,044 days).

468

469 **5. Comparison between the model and the experimental data**

470 Figure 9 shows the seasonal variation in the muon flux data acquired in the period
471 between August 20, 2017- June 30, 2020. As was expected, the muon flux showed a
472 negative correlation between the ambient temperature and the muon flux, indicating that
473 the isobaric surface height effect is predominant in seasonal variations in the muon flux.
474 In this period there were not any specific extraterrestrial events (such as a Forbush
475 decrease) that could have affected the primary flux. The muon counts in each bin (bin
476 width = 3 days) ranged between 7×10^5 - 7.4×10^5 . The muon flux variations were
477 normalized to the value observed on August 20, 2017. The muon flux modeling results
478 with barometric and isobaric corrections are overlaid on this plot (red solid lines in Figure
479 9). The root mean square (RMS) of the deviations between the theoretical values and the
480 observational values is 0.987%. The measured seasonal variation in the muon flux is well
481 explained by combining the current barometric and isobaric correction models.
482



483
484 Figure 9. Seasonal variation in the muon flux data acquired in the period between August
485 20, 2017- June 30, 2020. The observation values (blue filled circles) and theoretical
486 values (red solid lines) are shown. The statistical errors associated with each data point
487 fit within the size of the circles. The barometric modelling errors are within the width of
488 the red solid lines. Black solid lines indicate the predicted flux without the barometric
489 correction.

490

491

492 **6. Limitations and potential improvements**

493 The RMS deviation of the observed muon flux variations from the DOF modeling results

494 (~1%) induces an error of ~60 m in the estimation of the muopause height with the DOF
495 technique. The DOF time resolution is 3 days. These characteristics, the accuracy and
496 time resolution, are both significantly lower than the accuracy and the time resolution that
497 can be attained with the GPS-loaded balloons (~5 m and 1 second). This is the main
498 limitations of the DOF approach in its current stage of development. These limitations
499 mainly come from (A) the statistics and (B) the modeling accuracy. Regarding factor (A),
500 the detector size needs to be enlarged to record more muon events. In order to confirm
501 this detector size effect, as the first step, the detector size will be increased to a double
502 size (4.5 m²) to verify whether precision really scales by 2^{0.5}, which would be a proof that
503 statistics limitation dominates over modeling uncertainty. Regarding factor (B), more
504 precise modeling developments with Monte Carlo (MC) simulations such as CORSIKA
505 and Geant4 may improve the accuracy. The current work is based on the assumption is
506 that the muons travel straight forwardly without experiencing scatterings; however, it
507 must be noted that after the muons are generated near the tropopause, they travel through
508 a material with a thickness equivalent to 20-meter water equivalent (m.w.e.) - 40 m.w.e.
509 for the muons arriving from an elevation angular region between 14 °- 32 °, having a
510 tendency to scatter to cause longer track lengths in the troposphere. This effect must be
511 taken into account in our future work to make improvements to factor (B). The
512 discrepancy between the balloon position and the muon generation region may also
513 influence how closely the compared data sets match. The muospheric layer thickness
514 seasonally oscillates, but its amplitude is likely to depend on location of the measurement
515 on the Earth since the near surface temperature is regionally varied. If the surface
516 temperature is different between the location underneath the ballon and the location
517 underneath the region of interest of the muopause, the muopause height in this region and
518 the balloon-based isobaric surface altitude will not coincide. Since the balloon's trajectory
519 is random, and it is difficult to control it, the next step in development is to compare the
520 DOF data with the satellite-based stratospheric sensing data.

521

522 **7. Conclusion**

523 In conclusion, a new muographic technique called DOF was proposed, and with this
524 technique, it was found that the muopause height interlocks with the isobaric surface
525 height in the upper troposphere and lower stratosphere. This work defined (A) the position
526 of the muopause and the layer span of the muosphere on the Earth; additionally, it was
527 shown that (B) the muopause is located in the lower stratosphere, (C) seasonal variations
528 in the muon flux are predominantly ruled by muopause dynamics, (D) muopause
529 dynamics can be visualized with DOF muography by taking advantage of directional

530 patterns of cosmic-ray muon's survival probabilities, and (E) muopause dynamics is
531 closely related with isobaric surface height variations in the lower stratosphere.

532

533 Muopause dynamics has the potential to contribute to research focused on the upper
534 tropospheric and lower stratospheric dynamics. In future studies, the potential of DOF
535 muography for application to studying the dynamical processes occurring in the upper
536 troposphere and lower stratosphere will be further investigated by performing related case
537 studies and making specific comparisons with other atmospheric climate datasets. The
538 next step would be spatiotemporal mapping of the muopause that would reflect
539 spatiotemporal variations in tropospheric convection depth.

540

541

542 REFERENCES

543 Adamson, P. et al. (MINOS Coll.: Observation of muon intensity variations by season
544 with the MINOS far detector, *Phys. Rev.*, D81, 012001,
545 doi:10.1103/PhysRevD.81.012001, 2010

546

547 Allkofer, O.C. *et al.* Cosmic ray muon spectra at sea-level up to 10 TeV. *Nucl. Phys. B*
548 **259**, 1-18 (1985).

549

550 Blackett, P. M. S. On the instability of the Barytron and the temperature effect of cosmic
551 rays. *Phys. Rev.* **54**, 973–974 (1938). <https://doi.org/10.1103/PhysRev.54.973>

552

553 Blumer *et al.* Atmospheric Profiles at the Southern Pierre Auger Observatory and their
554 Relevance to Air Shower Measurement. Retrieved from [https://arxiv.org/abs/astro-](https://arxiv.org/abs/astro-ph/0507275)
555 [ph/0507275](https://arxiv.org/abs/astro-ph/0507275) (2005).

556

557 Boezio M. *et al.* New Measurement of the Flux of Atmospheric Muons. *Phys. Rev. Lett.*
558 **82**, 4757 (1999).

559

560 Boezio M. *et al.* Measurement of the flux of atmospheric muons with the CAPRICE94
561 apparatus. *Phys. Rev. D* **62**, 032007 (2000).

562

563 COSINE-100 Collaboration. Measurement of the cosmic muon annual and diurnal flux
564 variation with the COSINE-100 detector (2020). Retrieved from
565 <https://arxiv.org/abs/2005.13672>

566

567 Dmitrieva, A.N. *et al.* Corrections for temperature effect for ground-based muon
568 hodoscopes. *Astropart. Phys.* **34**, 401-411 (2011).

569

570 Gnanvo, K. *et al.* Imaging of high-Z material for nuclear contraband detection with a
571 minimal prototype of a muon tomography station based on GEM detectors. *Nucl. Instr.*
572 *Meth. A* **652**, 16-20 (2011).

573

574 Haino, S. *et al.* Measurements of primary and atmospheric cosmic-ray spectra with the
575 BESS-TeV spectrometer. *Phys. Lett. B* **594**, 35-46 (2004).

576

577 Japan Metrological Agency. Past Metrological Data (2023). Retrieved from
578 <https://www.jma.go.jp/jma/indexe.html>.

579

580 Kretschmer, M. *et al.* The different stratospheric influences on cold extremes in Eurasia
581 and North America. *npj Clim. Atmos.* **1**, 44 (2018).

582

583 L3 Collaboration. Measurement of the atmospheric muon spectrum from 20 to 3000 GeV.
584 *Phys. Lett. B* **598**, 15-32 (2004)

585

586 Millán, L. *et al.* The Hunga Tonga - Hunga Ha'apai Hydration of the Stratosphere,
587 *Geophys. Res. Lett.* **49**, e2022GL099381 (2022).

588

589 Morishima, K., Kuno, M., Nishio, A. *et al.* Discovery of a big void in Khufu's Pyramid
590 by observation of cosmic-ray muons. *Nature* **552**, 386–390 (2017).
591 <https://doi.org/10.1038/nature24647>

592

593 Myssowsky, L., & Tuwim, L. Unregelmäßige intensitätsschwankungen der
594 höhenstrahlung in geringer seehöhe. *Z. Phys.* **39**, 146–150 (1926).
595 <https://doi.org/10.1007/BF01321981>

596

597 Particle Data Group, The Review of Particle Physics. *Prog. Theor. Exp. Phys.* **2022**,
598 083C01 (2022).

599

600

601 Tanaka, H. K. M., Kusagaya, T. & Shinohara, H. Radiographic visualization of magma

602 dynamics in an erupting volcano. *Nat. Commun.* **5**, 3381 (2014).
603 <https://doi.org/10.1038/ncomms4381>
604

605 Tanaka, H.K.M., Aichi, M., Bozza, C. et al. First results of undersea muography with the
606 Tokyo-Bay Seafloor Hyper-Kilometric Submarine Deep Detector. *Sci Rep* 11, 19485
607 (2021). <https://doi.org/10.1038/s41598-021-98559-8>
608

609 Tanaka, H. K. M., Gluyas, J., Holma, M. *et al.* Atmospheric muography for imaging and
610 monitoring tropic cyclones. *Sci. Rep.* **12**, 16710 (2022a). <https://doi.org/10.1038/s41598-022-20039-4>
611

612

613 Tanaka, H. K. M., Aichi, M., Balogh, S.J. *et al.* Periodic sea-level oscillation in Tokyo
614 Bay detected with the Tokyo-Bay seafloor hyper-kilometric submarine deep detector (TS-
615 HKMSDD). *Sci. Rep.* **12**, 6097 (2022b). <https://doi.org/10.1038/s41598-022-10078-2>
616

617 The IceCube Collaboration. Seasonal variation of atmospheric muons in IceCube. *PoS*
618 (ICRC2019) 1177 (2019). Retrieved from <https://pos.sissa.it/358/894/>. RC2
619

620 Thompson, M. G. & Whalley, M. R. The sea-level muon spectrum and charge ratio and
621 their relationship with high-energy accelerator data. *J. Phys. G* **3**, 97 (1977).
622

623 Tilav, S. et al. Atmospheric variation as observed by IceCube (2010). Retrieved from
624 arXiv:1001.0776. -> This seems not have published elsewhere.
625

626 Tramontini, M., Rosas-Carbajal, M., Nussbaum, C., Gibert, D., Marteau, J. Middle-
627 Atmosphere Dynamics Observed With a Portable Muon Detector. *Earth and Space*
628 *Science* **6**, 1865-1876 (2019).
629

630 Vömel, H. *et al.* Water vapor injection into the stratosphere by Hunga Tonga-Hunga
631 Ha'apai, *Science* **377**, 1444–1447 (2022).
632

633 Yook, S. *et al.* Climate Impacts and Potential Drivers of the Unprecedented Antarctic
634 Ozone Holes of 2020 and 2021. *Geophys. Res. Lett.* **49**, e2022GL098064 (2022).
635 <https://doi.org/10.1029/2022GL098064>
636
637

638

639 **Data Availability**

640 The datasets used and/or analyzed during the current study are available from the
641 corresponding author on reasonable request.

642

643 **Author Contribution**

644 H.K.M.T. wrote the text. H.K.M.T. prepared the figures. H.K.M.T. reviewed the
645 manuscript.

646

647 **Competing interests**

648 The author is a member of the editorial board of Geoscientific Instrumentation, Methods
649 and Data Systems.

650

651

652

653

654